Journal Pre-proofs

Creating rich closed nanopores in anthracite-derived soft carbon enables greatly-enhanced sodium-ion storage in the low-working-voltage region

Jiawei Gu, Yiwei You, Miao Liu, Ling Huang, Zhefei Sun, Junjie Liu, Liyuan Sha, Minghui Chen, Sha Li, Shunqing Wu, Qiaobao Zhang, Li Zhang

PII: S1385-8947(25)00130-5
DOI: https://doi.org/10.1016/j.cej.2025.159331
Reference: CEJ 159331

To appear in: *Chemical Engineering Journal*

Received Date: 15 October 2024
Revised Date: 16 December 2024
Accepted Date: 5 January 2025

Please cite this article as: J. Gu, Y. You, M. Liu, L. Huang, Z. Sun, J. Liu, L. Sha, M. Chen, S. Li, S. Wu, Q. Zhang, L. Zhang, Creating rich closed nanopores in anthracite-derived soft carbon enables greatly-enhanced sodium-ion storage in the low-working-voltage region, *Chemical Engineering Journal* (2025), doi: https://doi.org/10.1016/j.cej.2025.159331

Creating Rich Closed Nanopores in Anthracite-Derived Soft Carbon Enables Greatly-Enhanced Sodium-Ion Storage in the Low-Working-Voltage Region

Jiawei Gu [a, ‡], Yiwei You [b, ‡], Miao Liu [a*], Ling Huang [a], Zhefei Sun [c], Junjie Liu [a], Liyuan Sha [a], Minghui Chen [a], Sha Li [d], Shunqing Wu [b,*], Qiaobao Zhang [c], Li Zhang [a,*]

[a]College of Chemistry and Chemical Engineering, State Key Laboratory of Physical Chemistry of Solid Surfaces, Tan Kah Kee Innovation Laboratory, Collaborative Innovation Center of Chemistry for Energy Materials (*i*ChEM), Xiamen University, Xiamen 361005, Fujian, China.

[b]Department of Physics, OSED, Key Laboratory of Low Dimensional Condensed Matter Physics (Department of Education of Fujian Province), Xiamen University, Xiamen 361005, China

[c]College of Materials, Xiamen University, Xiamen 361005, Fujian, China.

[d]Institute of Smart City and Intelligent Transportation, Southwest Jiaotong University, Chengdu, Sichuan, 611756, P. R. China.

‡ J. W. Gu and Y. W. You contributed equally to this work.

*Corresponding authors: Miao Liu (M.L.) liumiao11@xmu.edu.cn, Shunqing Wu (S.W.) wsq@xmu.edu.cn, Li Zhang (L.Z.) zhangli81@xmu.edu.cn

Abstract: Soft carbon, characterized by its abundant reserves, low cost, and high carbon yield, should have been an important choice for anode materials in sodium-ion batteries (SIBs), similar to hard carbon. However, traditional high-temperature synthesis tends to graphitize soft carbon, which is extremely detrimental to the adsorption and intercalation of Na^+ ions. This raises a highly challenging scientific question: whether it is possible to suppress the graphitization of soft carbon and transform it towards closed nanopores favorable for Na^+ storage during high-temperature treatment. Herein, we introduce flash Joule heating (FJH) technology to treat anthracite with rapid heating and quenching, obtaining metastable soft carbon (anthracite-FJH) containing a large number of short-range ordered graphitic microdomains and their assembled closed nanopores. Benefiting from the abundant closed nanopores, this kinetically-controlled soft carbon exhibits a significantly enhanced Na^+ adsorption and pore-filling capacity of 309 mAh g^{-1} at 0.1 C, dominantly contributed by the low-voltage plateau. Moreover, a reversible specific capacity of 256.2 mAh g^{-1} is maintained at 0.5 C with a capacity retention of 93.2% after 200 cycles. We experimentally and theoretically explicitly disclose the "carbon microstructure regulation-Na^+ storage mechanism" relationship. This work paves the way for the disruptive synthesis of high-capacity soft carbon SIB anodes based on anthracite.

Keywords: Anthracite-derived soft carbon; Sodium-ion battery anode; Abundant closed nanopore; Kinetically-controlled structural regulation; Enhanced sodium-ion storage

1. Introduction

Sodium-ion batteries (SIBs) are emerging as a highly promising alternative to lithium-ion batteries, largely due to the comparable properties of sodium to lithium, coupled with the abundance and accessibility of sodium resources.[1-3] As the core component of SIBs, the anode plays a crucial role in determining the overall cell performance.[4, 5] Unlike the commercial graphite anode used in lithium-ion batteries, the thermodynamics of Na^+ ions insertion into graphite to form binary graphite intercalation compound are unfavorable.[6, 7] To date, various

anodes based on intercalation, conversion, alloying, conversion-alloying and functional group mechanisms have been developed to achieve high capacity and long lifespan of SIBs,[8, 9] Among them, non-graphitizable carbon, especially hard carbon has become the primary choice for SIB anode owing to its comprehensive performance advantages.[10, 11] However, the drawbacks of traditional thermosetting precursors (*e.g.*, biomass,[12] polymers,[13] fossil fuels[8] and resins[14]), including high cost and low carbon yield, greatly hinder the practical application of hard carbons in SIBs.[15-17]

Recently, soft carbon precursors, such as anthracite,[17] asphalt,[18] and petroleum,[19] especially anthracite,[20] have been widely explored for SIB anodes due to its advantages of abundant reserves, low cost, and high carbon yield. Nevertheless, due to the condensed aromatic ring structure of anthracite, its direct pyrolysis will continuously transition towards highly ordered graphite as the temperature rises, and the interlayer spacing will gradually decrease.[20] Worse still, this highly graphitized soft carbon is neither conducive to the adsorption of Na^+ ions at defect sites nor favorable for the effective interlayer intercalation of Na^+ ions, thus it typically exhibits a sodium storage capacity that is significantly lower than that of hard carbon.[21] Despite the controversy, the current mechanisms for Na^+-ion storage in carbon structures are mainly based on: the ad-/chemisorption of Na^+ ions at defect sites and open surfaces in a voltage range between 1.0 and 0.1 V, as well as filling of Na^+ ions into closed nanopores in a low-voltage plateau below 0.1 V.[22-25] Apparently, to enhance the sodium storage capacity of anthracite-derived soft carbon, it is essential to effectively suppress the excessive graphitization tendency of soft carbon during the high-temperature process and to precisely regulate the carbon microstructures to create more closed nanopores.

In response, various effective strategies have been proposed to inhibit graphitization and synthesize unconventional soft carbon, including: I) Pre-oxidation treatment to inhibit the formation and growth of graphite microdomains.[26] II) Pre-polymerization to increase the spatial cross-linking degree of soft carbon and inhibit graphitization,[27] and III) Controlling the carbonization state (*e.g.*, transitioning from fusion-state to solid-state) or adjusting the heat-treatment temperature to regulate the degree of graphitization.[28] Although these methods have enhanced the Na^+ storage of soft carbon to a certain extent, the suppression effect on graphitization tendency is still very limited. More importantly, the Na^+ filling capacity of soft carbon below 0.1 V is still quite low owing to the limited pore-forming ability, leaving a large room for improvement. Therefore, it is urgent to develop transformative high-temperature treatment technologies that can suppress the ordered arrangement tendency of carbon atoms in soft carbon through kinetic control, and form topological closed pore structures to significantly increase the Na^+ storage capacity in the low-voltage region.

Herein, we have introduced flash Joule heating (FJH) technology that can achieve "shock heating" and "rapid cooling" to treat anthracite with controlled temperature and pulse width. Under instantaneous thermal pulses, carbon atoms in anthracite struggle to transform into thermodynamically controlled, long-range ordered graphitic microdomains. Instead, they tend to form kinetically controlled, short-range ordered topological turbostratic structures (*i.e.*, closed nanopores). Apparently, the obtained metastable anthracite-derived soft carbon (denoted as anthracite-FJH) can provide a large number of active sites for Na^+ filling in the low-voltage region (**Fig. 1a**). As such, the anthracite-FJH anode demonstrates a high capacity of 309 mAh g^{-1} at 0.1 C, including a plateau capacity of 69.9% in the low-voltage range, which is far higher than that of anthracite-derived soft carbon prepared by traditional tubular furnace heating (abbreviated as anthracite-TF, **Fig. 1a**). Moreover, a reversible capacity of 256.2 mAh g^{-1} is maintained at 0.5 C after 200 cycles with a capacity retention of 93.2%. Combining experimental characterization with machine learning simulations, we confirmed that anthracite-

FJH is rich in turbine-like closed nanopores and elucidated that Na^+ storage mechansim is mainly filled in nanopores in the form of quasi metallic clusters. More importantly, machine learning specifically clarifies the coupling relationship between the lateral size (L_a), stacking height (L_c), and interlayer spacing ($d_{(002)}$), as well as their impact on electrochemical performance. Benefiting from its high capacity at low potential region, the as-constructed full cell, employing anthracite-FJH as anode and $Na_3V_2(PO_4)_3$ (NVP) as cathode, delivers a high energy density of 225.3 Wh kg^{-1}. Our work has opened the door to the application of anthracite-derived soft carbon as the high-capacity SIB anode.

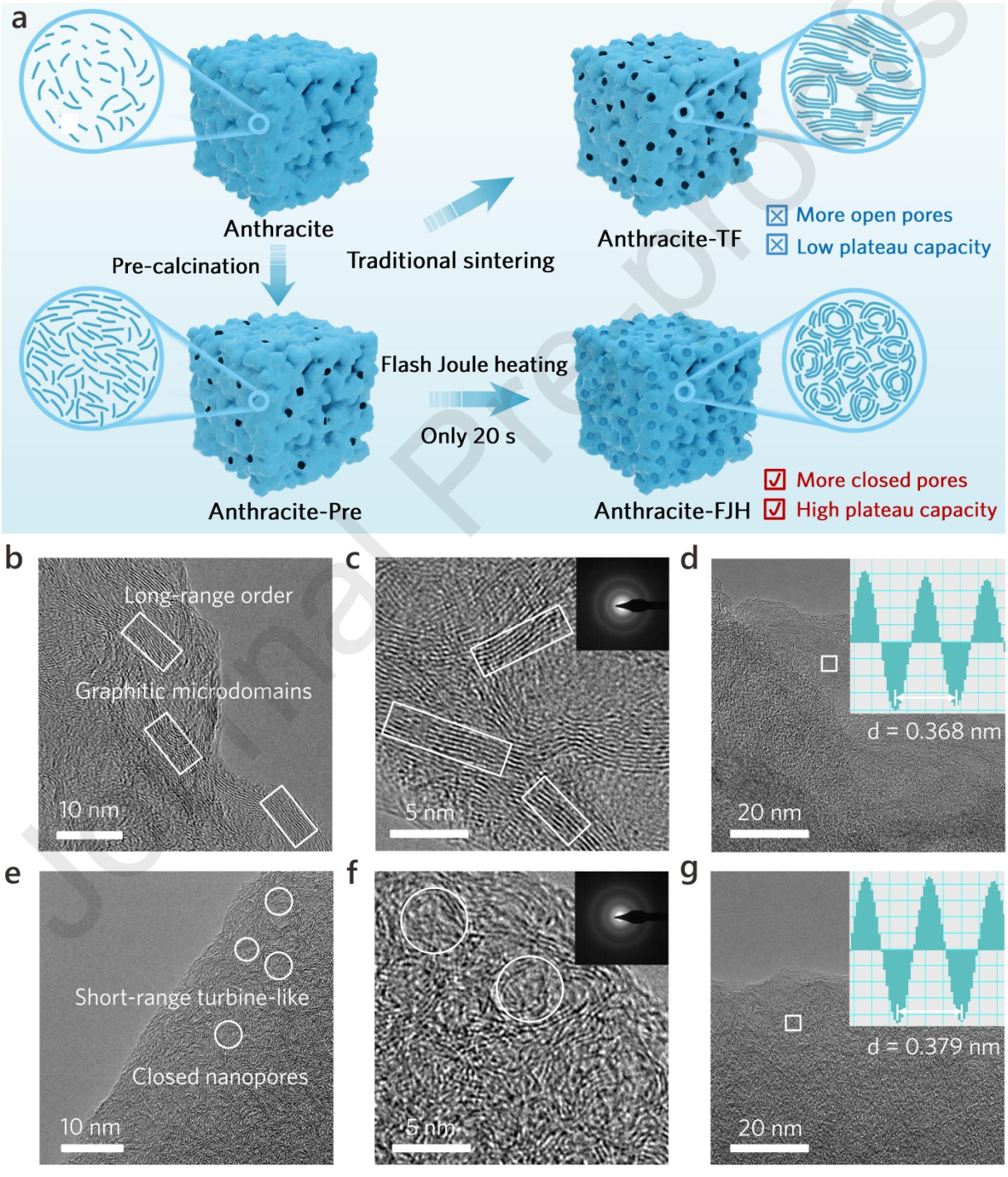

Figure 1. Preparation principle and microstructure characterization of metastable anthracite-derived soft carbon. (a) Schematic illustration of the structural differences between anthracite-derived soft carbons obtained through traditional tubular furnace heating (anthracite-TF) and flash Joule heating (anthracite-FJH). HRTEM of anthracite-TF (b, c) and anthracite-FJH (e, f) at different magnifications, inset of corresponding SAED pattern. Interlayer spacing of (d) anthracite-TF and (g) anthracite-FJH, respectively.

2. Results and Discussion

2.1. Synthesis and Microscopic Characterization of Anthracite-FJH Rich in Closed Nanopores

Fig. 1a schematically compares the preparation and structural differences between anthracite-derived soft carbons obtained through traditional tubular furnace heating and flash Joule heating. Firstly, high-purity anthracite was obtained by pulverizing and removing impurities originated from coarse anthracite. The subsequent low-temperature pre-carbonization induced the initial reorganization of carbon atoms within anthracite (anthracite-Pre, 700 °C), enhancing conductivity and mitigating the effects of carbon decomposition.[29] The reason for choosing 700 °C as pre-sintering for the anthracite anode is shown in **Fig. S1** (Supporting Information). Then, flash Joule heating was further introduced to treat anthracite-Pre, which can promote the localized rearrangement of the carbon atoms and inhibit the stacking of the carbon layer through thermal shock (anthracite-FJH, 1300 °C, 20 s), thereby creating more closed nanopores with turbine-like structure. This structure can efficiently increase the Na^+ ions storage capacity in the low potential region. In stark contrast, the ordered stacking and high graphitization can be achieved through direct traditional tube furnace heating at 1300 °C for 2 h (anthracite-TF), which is unfavorable for the Na^+ ions storage. Notably, the preparation of anthracite-FJH requires only 20 s using flash Joule heating, a duration far shorter than those previously recorded for anthracite-based anodes (**Fig. S2**, Supporting Information).[17, 30-34]

The surface morphology of the samples has been thoroughly examined using scanning electron microscopy (SEM). From the SEM analysis, no differences are observed between anthracite-FJH (**Fig. S3a**, Supporting Information) and anthracite-TF (**Fig. S3b**, Supporting Information). Furthermore, the internal graphitic microdomain structure was studied using transmission electron microscope (TEM) in detail. As depicted in **Fig. 1b-c**, the TEM image of anthracite-TF exhibits pronounced long-range ordered graphitic microdomains, characterized by a high degree of graphitization. In sharp contrast, the anthracite-FJH exhibits a characteristic turbine-like structures (**Fig. 1e** and **Fig. S4**), featuring smaller graphite-like domains with curved short-range layers randomly distributed over larger scales. Specifically, detailed high-resolution TEM (HRTEM) analysis of anthracite-FJH (**Fig. 1f**) displays a higher abundance of closed nanopores compared with anthracite-TF, thereby providing more active sites for Na^+-ion storage. Furthermore, the weakened diffraction rings of anthracite-FJH (inset of **Fig. 1f**) in the corresponding selected area electron diffraction (SAED) patterns in comparison with those of anthracite-TF (inset of **Fig. 1c**) also indicate an enhanced disorder of the microstructure. Additionally, the interlayer spacings are determined to be 0.368 and 0.379 nm for anthracite-TF (**Fig. 1d**) and anthracite-FJH (**Fig. 1g**), respectively, demonstrating an expansion of the interlayer spacing by flash Joule heating, which is beneficial to the transport and storage of Na^+ ions.

2.2. Spectroscopic Characterization of the Structural Differences Between Anthracite-FJH and Anthracite-TF

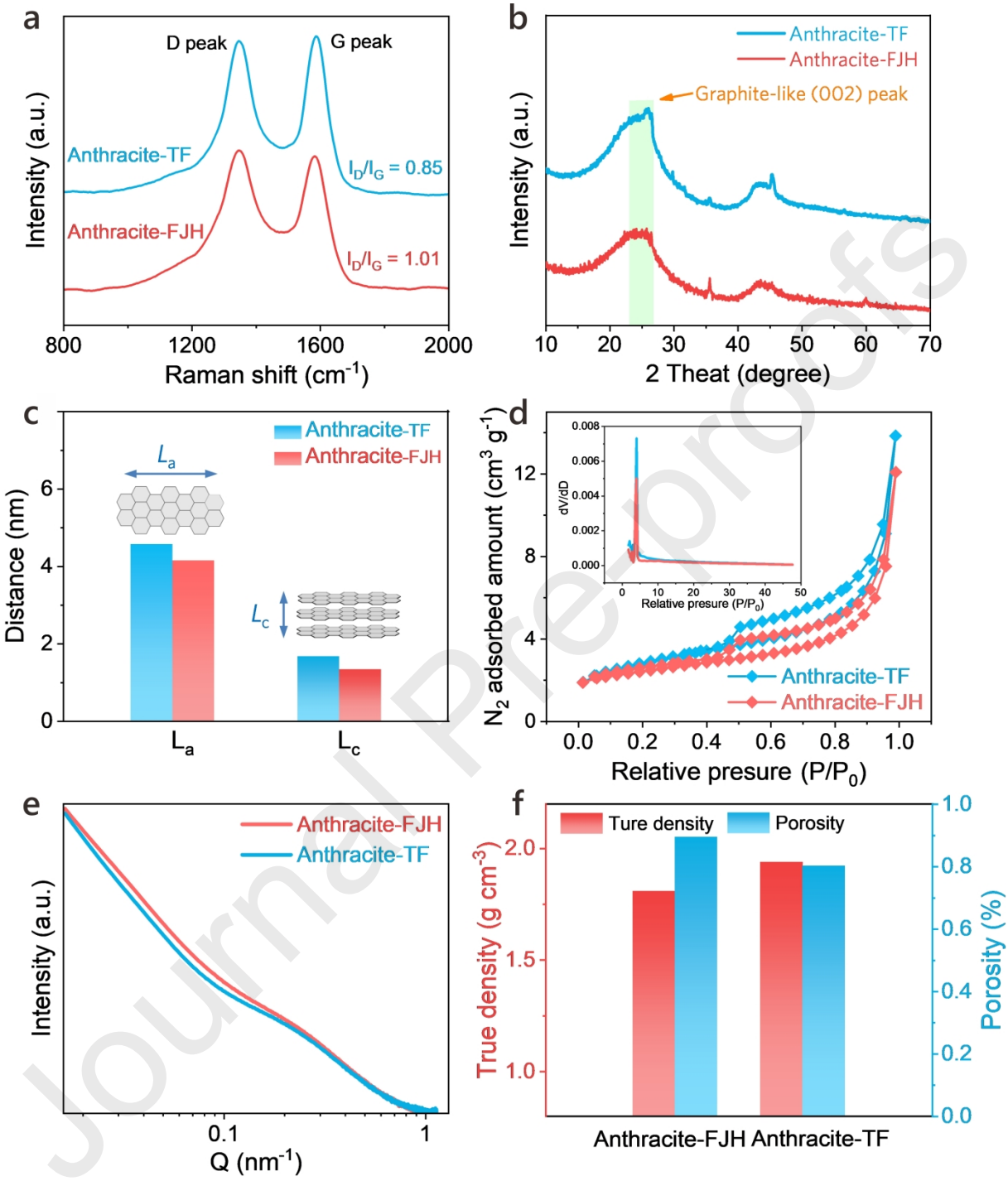

Figure 2. Spectroscopic analysis and porosity examination of anthracite-TF and anthracite-FJH. (a) Raman spectra and (b) XRD patterns of anthracite-TF and anthracite-FJH. (c) L_a and L_c values of anthracite-TF and anthracite-FJH. (d) Nitrogen adsorption/desorption isotherms of anthracite-TF and anthracite-FJH, inset of the corresponding NLDFT pore size distribution. (e) SAXS patterns and (f) Values of true density and porosity of anthracite-TF and anthracite-FJH.

The carbon crystallinity characteristics of both samples were further explored through X-ray diffraction (XRD) and Raman spectroscopy. As depicted in **Fig. 2a**, two typical peaks are

observed at 1350 and 1580 cm^{-1}, corresponding to the defect peak (D band) and graphite peak (G band), respectively.[29, 35, 36] Moreover, the I_D/I_G ratio directly reflects the degree of graphitization and defects.[37] Compared to anthracite-TF, anthracite-FJH exhibits a higher I_D/I_G value of 1.01, suggesting reduced graphitization and more disordered structures, which aids in adsorbing a greater number of Na^+ ions in the slope region. Based on the XRD patterns (**Fig. 2b**), it is evident that two broad diffraction peaks located at 23° and 43° correspond to the crystallographic planes of (002) and (100) in carbon materials.[35] Additionally, there is a smaller graphite-like peak located at 26° for anthracite-TF, indicating a high degree of graphitization. It can be observed that in anthracite-FJH, the (002) peak shifts to a lower angle compared to anthracite-TF, indicative of increased d-spacing ($d_{(002)}$). According to Bragg equation, anthracite-FJH delivers a larger interlayer spacing (**Fig. S5,** Supporting Information), facilitating fast transport and storage of Na^+ ions between layers[38], which is highly consistent with the HRTEM analysis. Meanwhile, L_a (length) and L_c (width) of carbon microcrystals are further calculated from the fitted XRD patterns (**Fig. 2c**), where both L_a and L_c values exhibit a decreasing trend from anthracite-TF to anthracite-FJH, indicating the lower degree of graphitization of anthracite-FJH achieved through flash Joule heating.

To comprehensively understand the effect of flash Joule heating on the surface area and pore structure in anthracite-based soft carbon, the evolution of the detailed pore structure is further characterized. Firstly, N_2 adsorption-desorption measurements have been executed to characterize the open pore structure for both samples, as depicted in **Fig. 2d**. Based on the Brunauer-Emmet-Teller (BET) model, the surface area of anthracite-FJH is measured to be 8.1 $m^2\ g^{-1}$, lower than that of anthracite-TF (9.7 $m^2\ g^{-1}$), indicating a reduced open pore structure in anthracite-FJH. The results suggest that flash Joule heating can regulate the pore structure of anthracite-based soft carbon to some extent. Secondly, further detailed structure of total pores number in both samples is evaluated using small-angle X-ray scattering (SAXS) technique. As shown in **Fig. 2e** and **Fig. S6**, SAXS pattern of anthracite-FJH displays enhanced scattering intensities around the scattering vector (Q) of 0.1 nm^{-1} as compared to anthracite-TF, thus indicating a higher number of closed pores in anthracite-FJH. By subtracting the BET area from the SAXS-fitted specific surface area, the surface area of closed nanopores in anthracite-FJH can be calculated as 97.5 $m^2\ g^{-1}$ (**Fig. S7,** Supporting Information), which is significantly higher than that of anthracite-TF (30.2 $m^2\ g^{-1}$). Meanwhile, true density and porosity are measured in anthracite-FJH shown in **Fig. 2f**, demonstrating an abundant closed pore structure prepared by flash Joule heating. All the detailed values of those tests have been added in **Table S1** (Supporting Information). Given the above, the flash Joule heating, distinct from traditional high-temperature heating, can be effectively employed to suppress the graphitic microdomain structure in soft carbon, accelerating the formation of more closed nanopores. This enhancement is expected to significantly boost the pore filling capacity of Na^+ ions below 0.1 V.[37, 38]

2.3. Anthracite-FJH Anode Enables Greatly-Enhanced SIB Half Cells and Full Batteries

As manifested in **Fig. 3a**, the first-cycle galvanostatic charge-discharge (GCD) profiles of anthracite-TF and anthracite-FJH can be divided into two major regions: a sloping region (above 0.1 V) and a plateau region (below 0.1 V). The reversible capacity of anthracite-FJH is 341 mAh g^{-1} at 0.02 C with a high ICE of 87.8%, significantly higher than that of anthracite-TF (252 mAh g^{-1}, 85.6%). The increased ICE for anthracite-FJH is ascribed to its lower surface area, as evidenced by BET analysis. Moreover, it can be seen that the enhanced capacity in anthracite-FJH primarily originates from the plateau region, accounting for 69.9% of the total capacity. This result indicates that the formation of abundant closed nanopores through flash Joule heating plays an important role in enhancing the Na^+-ion storage in soft carbon.[20]

Meanwhile, **Fig. S8,** Supporting Information illustrates the cyclic voltammetry (CV) curves of both samples, wherein a scan rate of 0.1 mV s^{-1} is employed within a potential range of 0.01-3 V. Note that a broad cathodic peak of anthracite-TF is located at around 0.4 V (**Fig. S8a**, Supporting Information), which is associated with the formation of irreversible solid electrolyte interface (SEI) film stemming from its high open pore surface area,[15] and this peak disappears in the subsequent cycles. Unlike anthracite-TF, anthracite-FJH exhibits more pronounced redox peaks at lower potentials due to its larger plateau capacity (**Fig. S8b**, Supporting Information), maintaining good overlap after the first cycle, indicating favorable reversibility of the electrochemical reactions.

More importantly, as shown in **Fig. 3b**, anthracite-FJH delivers a higher reversible capacity compared to anthracite-TF within a potential range of 0.01-3 V at 0.02 C for the initial two cycles. When the current density increases to 0.1 C, a reversible capacity of ~327.8 mAh g^{-1} for anthracite-FJH is received over 80 cycles without any capacity decay, higher than that of anthracite-TF. Moreover, the corresponding GCD profiles (**Fig. S9,** Supporting Information) of anthracite-FJH are well overlapped with each other for various cycles, along with distinct plateau regions at lower voltage range, indicating its favorable capacity retention and superior cyclability for the sodium ion storage. Furthermore, the anthracite-FJH anode demonstrates an advanced rate capability at various current densities ranging from 0.02 C to 5 C (**Fig. 3c**), significantly surpassing that of anthracite-TF. For example, a reversible capacity as high as ~202.2 mAh g^{-1} is retained at 5 C, while maintaining the obvious plateau below 0.1 V than anthracite-TF. Also, upon returning the current density to 1 C, 0.5 C and 0.2 C, the corresponding capacity retention of 99.8%, 98.4% and 98.9% are received, respectively, indicative of an excellent reversibility even after high rates. The difference in electrochemical performance between anthracite-FJH and anthracite-TF can be attributed to the disordered, turbine-like closed nanopores formed in Anthracite-FJH under FJH technology. These nanopores significantly enhance the sodium-ion storage capacity, which is primarily filled in the form of quasi-metallic clusters at the low-voltage plateau.

GCD profiles of both electrodes at varying rates are depicted in **Fig. S10**, Supporting Information. The nearly ~0 mAh g^{-1} for anthracite-TF is seen at high rates below 0.1 V. In contrast, the GCD profiles of anthracite-FJH remain almost unchanged even at high rates, especially below 0.1V, indicating that the generated closed nanopores are conducive to enhancing Na^+ ion storage.[39-41]. Notably, as depicted in **Fig. 3d**, the long-term cycling stability of anthracite-FJH is recorded with a higher reversible capacity of 275.3 mAh g^{-1} compared to anthracite-TF, maintained over 200 cycles at 0.5 C, achieving a capacity retention of 93.2% (**Fig. S11**, Supporting Information). In particular, the specific capacity and ICE of anthracite-FJH in this work have exceeded those of a series of anthracite-based soft carbon anodes recorded in Na-ion half cells so far (**Fig. 3e**).[17, 31, 32, 37, 42, 43]

Benefiting from the outstanding performance in the half cell, a full SIB battery is assembled by employing anthracite-FJH as anode and NVP as cathode (**Fig. 3f**), respectively. To ensure the overall performance of the full cell, a mass ratio of 2:5 for anthracite-FJH to NVP is utilized, according to their specific capacities. Note that the as-constructed full cell displays an average working voltage of 3.41 V (**Fig. 3g**). The anthracite-FJH//NVP full cell delivers a superior rate capability, achieving a high capacity of 62.8 mAh g^{-1} at 6 C. Meanwhile, the anthracite-FJH//NVP full cell exhibits an impressive long-term cycling performance, maintaining a high specific capacity of 108.7 mAh g^{-1} with a 64.5% capacity retention after 100 cycles (**Fig. 3h**). The energy density of the constructed full cell, calculated from the total mass of the anode and cathode active materials, reaches 225.3 Wh kg^{-1}, indicating the significant application potential of anthracite-FJH for practical SIBs.

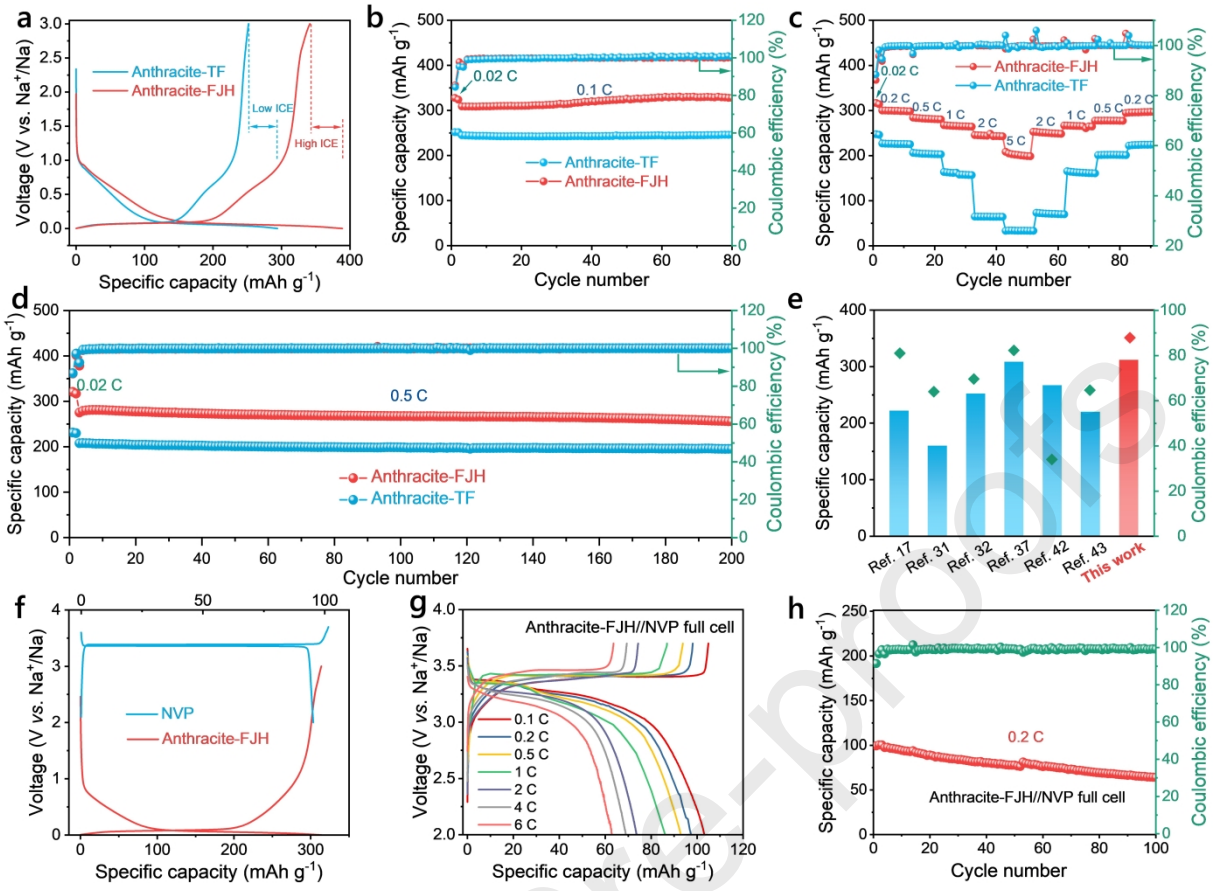

Figure 3. Electrochemical performance of anthracite-TF and anthracite-FJH anodes in SIB half and full cells. (a) Representative GCD profiles in the potential range of 0.01-3 V at 0.02 C. (b) Cycling performance at 0.1 C. (c) Rate capability at various rates ranging from 0.2 C to 5 C. (d) Long-term cycling performance at 0.5 C. (e) Comparison of specific capacity and ICE for anthracite-FJH with previous anthracite as anodes for SIBs reported in literatures. (f) GCD profiles of a full cell using anthracite-FJH anode and $Na_3V_2(PO_4)_3$ cathode. (g) GCD profiles of anthracite-FJH//NVP full cell at various current rates. (h) Cycling performance of the anthracite-FJH//NVP full cell at 0.2 C.

Given the above, it is indicated that the flash Joule heating has been successfully incorporated into the preparation of anthracite-based soft carbon to accurately regulate the localized graphitization and effectively capture microstructure in the metastable stage, which restrains the stacking of carbon layers, thus receiving the abundant closed nanopore structure and high reversible capacity in the low working voltage region.

2.4. In-Depth Characterizations of Na^+-Storage Mechanism in Anthracite-FJH

In situ Raman and *in situ* XRD measurements are employed to deeply probe the sodium ion storage mechanism of anthracite-FJH. **Fig. 4a** presents the *in situ* Raman spectra of anthracite-FJH in the first discharge-charge cycle at 0.5 C. It is evident that during the discharge process, the potential gradually decreases as Na^+ ions are adsorbed and gradually fill the defect sites, thereby reducing the number of defect sites in the carbon material. This leads to a decrease in the electron cloud density, which lowers the electronic resonance between carbon atoms (**Fig. 4b**) and causes the intensity of the D peak to weaken (**Fig. 4c**). Meanwhile, the G peak wavenumber shifts from 1581.1 cm^{-1} to 1559.1 cm^{-1}. During the charging process, Na^+ ions are

gradually extracted, and the D peak intensity and G peak Raman shift gradually recover. This process is highly reversible.

The sodium ion storage mechanism of anthracite-FJH has further been investigated by *in situ* XRD. As displayed in **Fig. 4d-f**, there is no significant shift observed in the (002) peak during the sodiation process, implying negligible Na^+ intercalation behavior between graphitic layers in both the sloping and plateau regions.[37, 44] Integrating *in situ* Raman and *in situ* XRD results, the sodium ions storage mechanism of anthracite-FJH can be described as adsorption-filling, wherein sodium ions are adsorbed at defect sites and subsequently filled into closed pores. Furthermore, *ex situ* TEM was executed to analyze the form of metallic sodium formed for both electrodes after discharging to 0 V. Compared to anthracite-TF (**Fig. 4g**), a clearer observation of numerous metallic sodium clusters is evident for anthracite-FJH (**Fig. 4h**). Additionally, diffraction points are corresponding to the (110) and (200) crystal planes of metallic sodium. This result confirms the formation of metallic sodium clusters within closed pores.[41] To further demonstrate the filling behavior of Na^+ ions within closed pores, anthracite-FJH was discharged to different voltage states (vs. Na^+/Na) after being immersed in an ethanol solution containing 1% phenolphthalein (**Fig. 4i**). Obviously, the color of ethanol phenolphthalein solution gradually darkens, reaching its deepest hue upon discharging to 0 V. Also, it delivers a darker red color compared to anthracite-TF (**Fig. S12,** Supporting Information). What convincingly confirms is that the capacity below 0.1 V is indeed generated by filling the closed pores with metallic sodium. Furthermore, it is noteworthy that the charged electrode no longer makes the solution red, which suggests the complete reversion of metallic sodium to its cationic state, thereby highlighting the high reversibility of pore-filling process.[23]

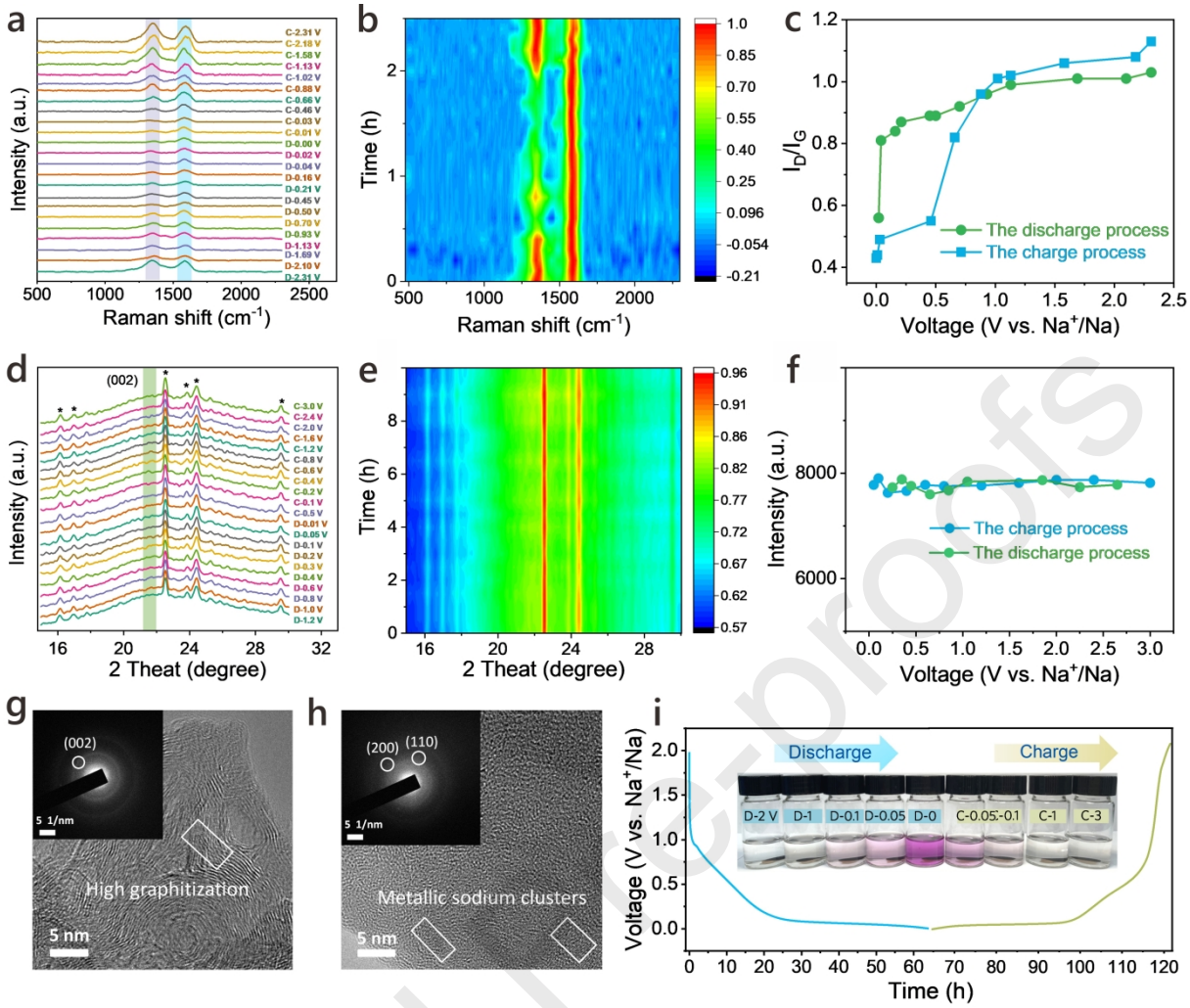

Figure 4. ***In situ*** **characterization of anthracite-FJH anode throughout the entire sodiation/de-sodiation process.** *In situ* Raman spectra for (a) corresponding curves and (b) contour mappings as well as (c) the ratio of I_D/I_G during cycling. *In situ* XRD patterns for (d) relevant curves and (e) contour mappings as well as (f) the change of intensity during cycling. HRTEM and inset of SAED images for (g) anthracite-TF and (h) anthracite-FJH at the electrochemical stage of sodiation. (i) GCD profiles and change in the color of anthracite-FJH soaked in phenolphthalein at various stages of charge and discharge.

The reaction kinetics of both electrodes have been characterized by *in situ* electrochemical impedance spectroscopy (EIS) and galvanostatic intermittent titration technique (GITT). As illustrated in **Fig. 5a-b**, all the EIS curves consist of two semicircles and a sloping line, corresponding to the solid electrolyte interface films resistance (R_{SEI}) and charge transfer resistance (R_{ct}) in the high-frequency and Warburg resistance in the low-frequency region, respectively.[45, 46] It is noteworthy that anthracite-FJH demonstrates a lower R_{ct} (~20 Ω) throughout the sodiation/de-sodiation process (**Fig. 5c**). This reduction is particularly pronounced in the low-working-voltage region, where the observed R_{ct} in anthracite-FJH is significantly lower than that of anthracite-TF, indicative of rapid Na-filling behavior within closed nanopores. Furthermore, the activation energy can be calculated to explore the reaction energy barrier of both electrodes using temperature-dependent EIS (**Fig. S13**, Supporting Information) based on the Arrhenius equation (inset of **Fig. 5d**).[47] The E_a of anthracite-FJH and anthracite-TF are 9.76 kJ mol^{-1} and 26.49 kJ mol^{-1}, respectively, where such the lower E_a in anthracite-FJH endows fast reaction rate during the electrochemical process.

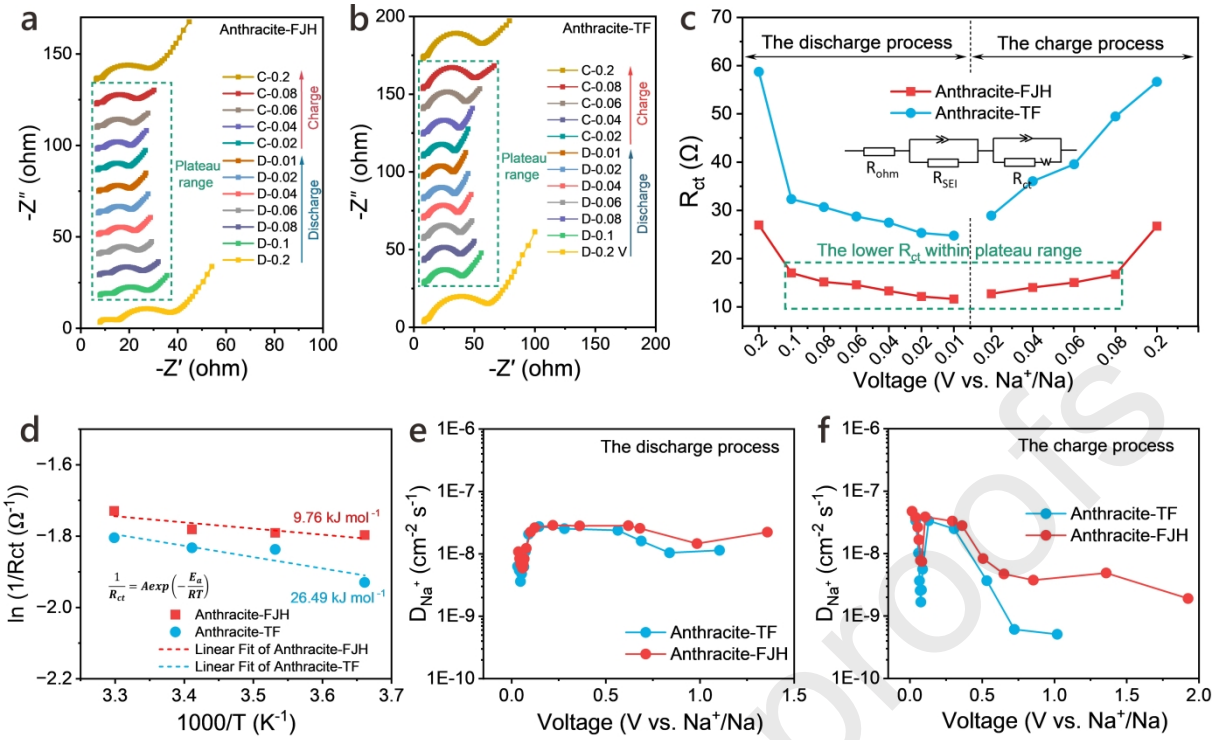

Figure 5. Kinetic characterization of anthracite-TF and anthracite-FJH electrodes at various stages of charge and discharge. *In situ* EIS of (a) anthracite-FJH and (b) anthracite-TF with an amplitude of 10 mV in the frequency range from 0.01 Hz to 100 KHz at 0.5 C. (c) Value statistics of charge transfer resistances (R_{ct}) from the Nyquist plot at the whole sodiation/de-sodiation process. (d) Activation energy of both electrodes calculated by temperature-dependent EIS. Na-ion diffusion coefficient (D_{Na+}) of both electrodes during the (e) discharge and (f) charge processes.

Moreover, GITT analysis was employed to probe the Na-ion diffusion coefficient (D_{Na+}) based on Fick's second law (**Fig. S14** and **Fig. S15**, Supporting Information) upon cycling, using a pulse current of 50 mA g^{-1} for 10 min with a duration of 40 min.[47] As disclosed in **Fig. 5e-f**, the high diffusivity of Na^+ ions are observed within the slope region, accompanied by slight variation, which corresponds to their adsorption onto the carbon surface. Following this, there is a pronounced decrease in D_{Na+} around 0.1-0.05 V, attributed to the intercalation of Na^+ ions through the carbon layer and into the interior of anthracite-FJH. While the reversal observed in D_{Na+} below 0.05 V can be attributed to starting of sodium ions filling the nanopores. What is mentioned that, both in the slope region and plateau region, anthracite-FJH exhibits a higher D_{Na+} than anthracite-TF. To further comprehend sodium storage behavior, the reaction kinetics have been analyzed by recording CV curves at different scan rates (**Fig. S16a**, Supporting Information). It is observed that the peak current of the anthracite-FJH electrode exhibits a more pronounced increase with the scan rate compared to anthracite-TF electrode (**Fig. S17a**, Supporting Information). The *b* values in anthracite-FJH (**Fig. S16b**, Supporting Information), derived from the relationship ($i = av^b$) between peak current (i) and scan rate (v), is found to be 0.66, surpassing that of anthracite-TF[39] (b=0.54, **Fig. S17b**, Supporting Information). The higher *b* value suggests that the reaction kinetics of anthracite-FJH are faster than anthracite-TF, both in terms of diffusion-controlled plateau capacity and surface-controlled slope capacity.[48] All in all, the regulation of abundant closed nanopore structure is achieved using flash Joule heating on soft carbon, thereby facilitating rapid Na^+ transportation and enhancing reaction kinetics, which is responsible for the superior rate capability.

2.5. Machine-Learning Simulation of Na^+-Storage Mechanism in Anthracite-FJH

Moreover, in order to determine the appropriate flash duration and temperature, a series of comparative experiments are conducted, as depicted in **Fig. S18-S20**, Supporting Information. It is evident that regardless of the temperature or heating duration, anthracite produced via flash joule heating exhibits a higher capacity compared to that synthesized using a traditional tube furnace. Interestingly, with the pulse duration held constant, the discharge capacity of anthracite-FJH initially increases and then decreases with rising temperature. Likewise, with the pulse temperature maintained constant, the discharge capacity of anthracite-FJH first increases and then decreases with increasing pulse duration. Thus, the optimal pulse temperature and duration have been determined as 1300 ℃ and 20 s, corresponding to suitable L_a, L_c and layer spacing.

Molecular dynamics simulations using a machine learning potential were performed to explore the impact of structural parameters on electrochemical properties.[41] **Figure 6a-b**, based on experimental data from anthracite-FJH and anthracite-TF, respectively, present two models illustrating the insertion positions of Na^+ ions at different voltages. Each model consists of three stages, with each stage corresponding to a different voltage range (as shown in **Fig. 6e**).

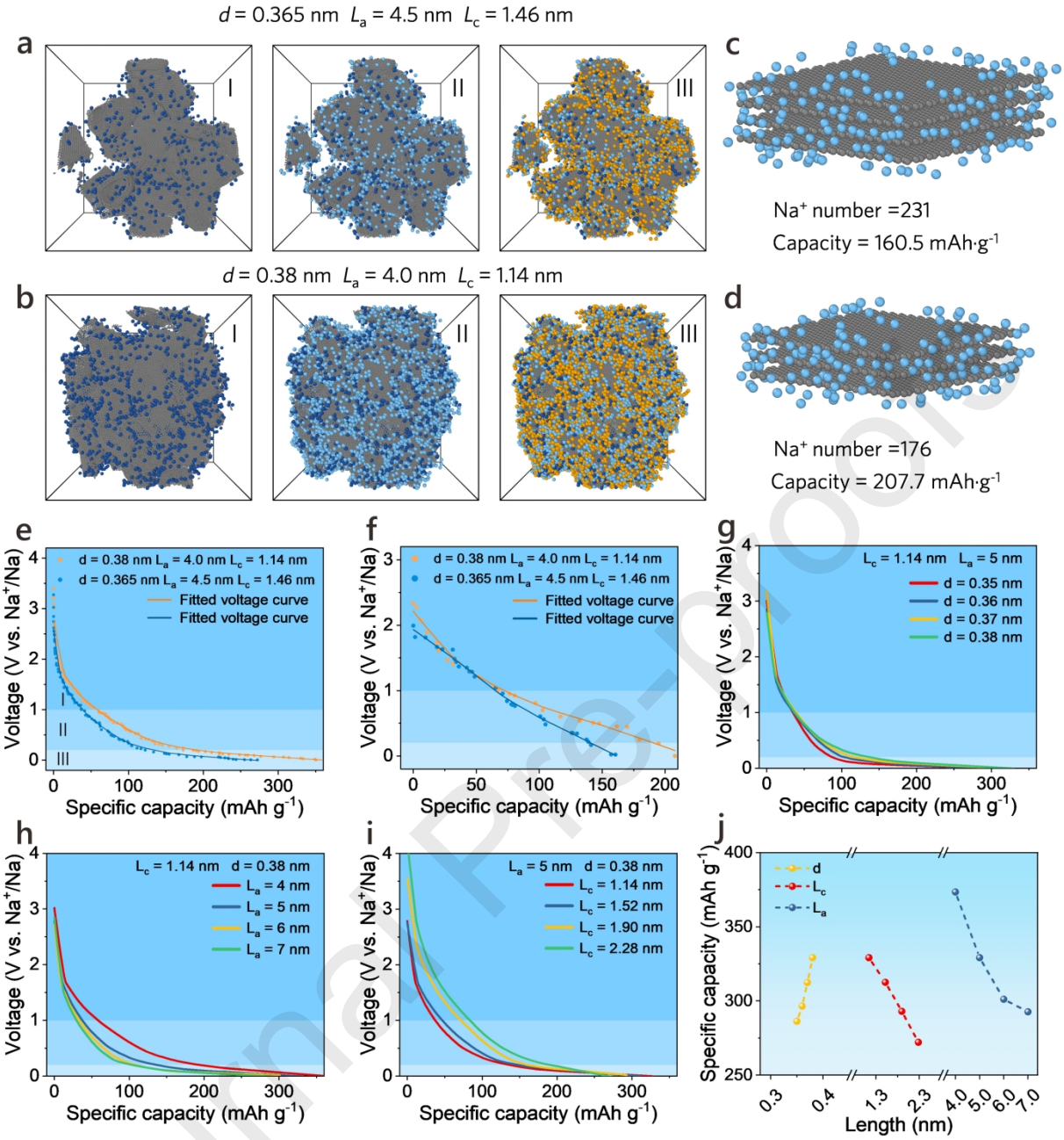

Figure 6. Effects of different structural parameters on voltage and capacity. (a, b) Structural diagrams of different Na-embedded stages. (c, d) Structural diagrams of Na-embedded monolithic carbon layers. (e) Voltage curves of models a and b. (f) Voltage curves of models c and d. (g) Voltage curves corresponding to different d. (h) voltage curve corresponding to different L_a. (i) Voltage curves corresponding to different L_c. (j) The relationship between three parameters and discharge capacity.

In Stage I, Na^+ ions primarily adsorb at the edges of carbon layers and are difficult to detach, corresponding to a higher voltage region. After the Na^+ ions are adsorbed in Stage I, additional Na^+ ions can easily continue to adsorb in surrounding areas, which corresponds to the voltage range of Stage II. Based on the first two stages, the Na^+ ions that follow tend to cluster (represented as yellow-brown spheres) near the original adsorption sites or in the voids between carbon layers, as confirmed by ex-situ TEM analysis. **Fig. 6c-d** show the capacities for fully embedded Na^+ ions in monolithic carbon under two different parameter sets. As shown in **Fig.**

6e, carbon layers with larger L_c values adsorb more Na^+ ions. However, higher L_a and L_c values imply more carbon atoms, which actually reduces the specific capacity, as depicted in **Fig. 6f**.

Further investigation into the relationships between L_a, L_c, d, and discharge capacity revealed several trends. When L_a and L_c remain constant, an increase in d significantly boosts capacity in the sloping region (**Fig. 6g**), attributed to the larger interlayer spacing providing more edge adsorption sites. Conversely, when only L_a or L_c varies, an increase in either parameter results in a decline in capacity in the sloping region (**Fig. 6h-i**), because increasing L_a or L_c can only increase a small amount of Na adsorption, but significantly raises the number of carbon atoms, thereby lowering the specific capacity. In summary, **Fig. 6j** outlines the influence of these three parameters on capacity.

3. Conclusion

In summary, we have successfully suppressed the graphitization tendency of anthracite-derived soft carbon at high temperatures by introducing a kinetically controlled flash sintering strategy, transforming it into a metastable structure rich in closed nanopores. The as-obtained anthracite-FJH soft carbon not only delivers a significantly enhanced sodium storage capacity of 309 mAh g^{-1}, but also the main capacity increase comes from the low voltage region below 0.1 V (216 mAh g^{-1} vs. 169 mAh g^{-1} of the anthracite-TF soft carbon). Meanwhile, the anthracite-FJH anode also exhibits an outstanding rate capability. We have experimentally and theoretically elucidated the mechanism for storing sodium ions in anthracite-FJH involves the adsorption of Na^+ ions around the slope region and the dominant pore filling of Na^+ ions in the low plateau region. Moreover, the pivotal role of high-plateau-capacity anthracite-FJH anodes in contructing high-energy-density anthracite-FJH//NVP full batteries up to 225.3 Wh kg^{-1} has been convincingly demonstrated. Our concept of instantaneously restructuring soft carbon involves shifting traditional easily graphitizable soft carbon towards a non-graphitizable direction, moving closer to hard carbon with better Na^+-ion storage performance. This work will greatly promote the large-scale preparation and commercial application of low-cost and high-capacity soft carbon anode materials in future SIBs.

4. Experimental Section

Materials synthesis: All chemicals were purchased from commercially-available sources and directly used as reagents. The purification process of anthracite contained three steps: Firstly, the coarse anthracite was pulverized in the breaking machine for 3 min, and then the obtained particles were passed through the 500-mesh screening machine to obtain anthracite with particles smaller than 30 μm. Secondly, the above product was immersed in 3 M NaOH and 3 M HCl solutions, respectively, and stirred for 6 h at room temperature, then rinsed with deionized water for several times until the pH became neutral. The obtained product was denoted as anthracite-OH/H. Thirdly, the anthracite-OH/H was dried at 100 °C for 8 h in a vacuum oven. The anthracite-FJH was synthesized through two steps: Firstly, the anthracite-OH/H was pre-carbonized in a tube furnace under argon flow at 700 °C for 2 h. Subsequently, the pre-carbonized product was wrapped in carbon fiber, placed in a Joule heating device equipped with a temperature control system and circulating cooling system, and treated with an instantaneous high temperature of up to 1300 °C for 20 s under argon atmosphere. The working voltage and current were set at 40 V and 42.5 A, respectively. As the reference, the anthracite-OH/H was pre-carbonized in a tube furnace under argon flow at 700 °C for 2 h and then carbonized in a tube furnace filled with argon gas at 1300 °C for 2 h, with a heating rate of 5 °C min^{-1}, and denoted as anthracite-TF.

Electrode preparation and battery assembly: The working electrode was prepared by homogeneously mixing the active materials, super-P (MTI Technology Co., Ltd) and sodium carboxymethyl cellulose (CMC) (MTI Technology Co., Ltd) binder in a weight ratio of 92:3:5, using water (Millipore system, 18.2 MΩ cm) as solvent. Then, the mixture was coated onto copper foil, and dried at 120 °C under vacuum for 12 h. The average mass loading of active material was 1~1.5 mg cm^{-2}, with the electrode disc diameter and thickness of 11 mm and 100 μm, respectively. To prepare the cathode, $Na_3V_2(PO_4)_3$, PVDF, and Super P are uniformly mixed in NMP solvent at a mass ratio of 9:0.5:0.5. After stirring for several hours, the mixture was coated onto aluminum foil and dried at 100 °C under vacuum for 12 h. All the batteries were assembled in coin-type cells (CR 2032) using Na metal foil and glass fiber (Whatman GF/D) as the counter electrode and separator, respectively. The electrolyte employed was 1 M $NaPF_6$ dissolved in diethylene glycol dimethyl ether (DIGLYME). The cells were fabricated in a glove box (MIKROUNA), with the oxygen (O_2) and water (H_2O) levels carefully maintained below 0.1 ppm.

Materials characterization, *electrochemical measurements and Training Details for Machine Learning Interatomic potential*: The characterization of material structure and morphology, as well as electrochemical measurements, are provided in the experimental section of the supplementary materials.

Acknowledgements

This work was supported by the National Natural Science Foundation of China (Grant Nos. 92372101, 52122211 and 21875155), the Fundamental Research Funds for the Central Universities (20720220010), the National Key Research and Development Program of China (2021YFA1201502). M. Liu acknowledges the support of China Postdoctoral Science Foundation (2024M751764). L. Zhang acknowledges the support of Nanqiang Young Top-notch Talent Fellowship in Xiamen University. S. Li acknowledges the support of Postdoctoral Fellowship Program of CPSF (Grant No. GZB20230608). We also thank Prof. Yongsheng Hu in Institute of Physics, Chinese Academy of Sciences, and Prof. Yanan Chen in Tianjin University for their helpful guidance.

Appendix A. Supplementary data

The following are the Supplementary data to this article.

Received: ((will be filled in by the editorial staff))
Revised: ((will be filled in by the editorial staff))
Published online: ((will be filled in by the editorial staff))

Reference

[1] W. Yan, Z. Mu, Z. Wang, Y. Huang, D. Wu, P. Lu, J. Lu, J. Xu, Y. Wu, T. Ma, M. Yang, X. Zhu, Y. Xia, S. Shi, L. Chen, H. Li, F. Wu, Hard-carbon-stabilized Li–Si anodes for high-performance all-solid-state Li-ion batteries, Nat. Energy 8 (2023) 800-813.

[2] Y. Li, A. Vasileiadis, Q. Zhou, Y. Lu, Q. Meng, Y. Li, P. Ombrini, J. Zhao, Z. Chen, Y. Niu, X. Qi, F. Xie, R. van der Jagt, S. Ganapathy, M.-M. Titirici, H. Li, L. Chen, M. Wagemaker, Y.-S. Hu, Origin of fast charging in hard carbon anodes, Nat. Energy 9 (2024) 134-142.

[3] Y. Li, F. Wu, Y. Li, M. Liu, X. Feng, Y. Bai, C. Wu, Ether-based electrolytes for sodium ion batteries, Chem. Soc. Rev. 51 (2022) 4484-4536.

[4] D.-Y. Lan, X.-F. Qu, Y.-T. Tang, L.-Y. Liu, J. Liu, Acetate solutions with 3.9 V electrochemical stability window, J. Electrochem 28 (2022) 2102231.

[5] Q. Jin, K. Wang, H. Li, W. Li, P. Feng, Z. Zhang, W. Wang, M. Zhou, K. Jiang, Tuning microstructures of hard carbon for high capacity and rate sodium storage, Chem. Eng. J. 417 (2021) 128104.

[6] X.-P. Yin, Y.-F. Zhao, J.-J. Zhang, Research progress and performance improvement strategies of hard carbon anode materials for sodium-ion batteries, J. Electrochem 29 (2023) 224301.

[7] S. Alvin, C. Chandra, J. Kim, Controlling intercalation sites of hard carbon for enhancing Na and K storage performance, Chem. Eng. J. 411 (2021) 128490.

[8] S. Ma, W. Yan, Y. Dong, Y. Su, L. Ma, Y. Li, Y. Fang, B. Wang, S. Wu, C. Liu, S. Chen, L. Chen, Q. Huang, J. Wang, N. Li, F. Wu, Recent advances in carbon-based anodes for high-performance sodium-ion batteries: Mechanism, modification and characterizations, Mater. Today 75 (2024) 334-358.

[9] B. Wang, Y. Yao, W. Wang, Y. Xu, Y. Sun, Q. Li, H. Hu, M. Wu, Identifying the plateau sodium storage behavior of hard carbon through the spin state, Chem. Eng. J. 488 (2024) 151055.

[10] Y. Zeng, J. Yang, H. Yang, Y. Yang, J. Zhao, Bridging microstructure and sodium-ion storage mechanism in hard carbon for sodium ion batteries, ACS Energy Lett. 9 (2024) 1184-1191.

[11] B. Zhong, C. Liu, D. Xiong, J. Cai, J. Li, D. Li, Z. Cao, B. Song, W. Deng, H. Peng, H. Hou, G. Zou, X. Ji, Biomass-derived hard carbon for sodium-ion batteries: basic research and industrial application, ACS Nano 18 (2024) 16468-16488.

[12] K.-L. Hong, L. Qie, R. Zeng, Z.-Q. Yi, W. Zhang, D. Wang, W. Yin, C. Wu, Q.-J. Fan, W.-X. Zhang, Y.-H. Huang, Biomass derived hard carbon used as a high performance anode material for sodium ion batteries, J. Mater. Chem. A 2 (2014) 12733-12738.

[13] X. Jin, W. Zhang, S. Liu, T. Zhang, Z. Song, W. Shao, R. Mao, M. Yao, X. Jian, F. Hu, Highly stable $Ti_3C_2T_x$ MXene-based sandwich-like structure via interfacial self-assembly of nitrogen-rich polymer network for superior sodium-ion storage performance, Chem. Eng. J. 451 (2023) 138763.

[14] Q. Wang, Z. Hu, R. Zhang, C. Fan, J. Liu, J. Liu, Anode of anthracite hard carbon hybridized by phenolic epoxy resin toward enhanced performance for sodium-ion batteries, ACS Appl. Energy Mater. 7 (2024) 6704-6716.

[15] X. Yao, Y. Ke, W. Ren, X. Wang, F. Xiong, W. Yang, M. Qin, Q. Li, L. Mai, Defect-rich soft carbon porous nanosheets for fast and high-capacity sodium-ion storage, Adv. Energy Mater. 9 (2018) 1803260.

[16] F. Xie, Z. Xu, A.C.S. Jensen, H. Au, Y. Lu, V. Araullo-Peters, A.J. Drew, Y.S. Hu, M.M. Titirici, Hard-soft carbon somposite anodes with synergistic sodium storage performance, Adv. Funct. Mater. 29 (2019) 1901072.

[17] Y. Li, Y.-S. Hu, X. Qi, X. Rong, H. Li, X. Huang, L. Chen, Advanced sodium-ion batteries using superior low cost pyrolyzed anthracite anode: towards practical applications, Energy Storage Mater. 5 (2016) 191-197.

[18] D. Sun, L. Zhao, P. Sun, K. Zhao, Y. Sun, Q. Zhang, Z. Li, Z. Ma, F. Zheng, Y. Yang, C. Lu, C. Peng, C. Xu, Z. Xiao, X. Ma, Rationally regulating closed pore structures by pitch coating to boost sodium storage performance of hard carbon in low-voltage platforms, Adv. Funct. Mater. 34 (2024) 2403642.

[19] J.H. Lv, J.S. Wang, B. He, T. Wu, A.H. Lu, W. Zhang, J. Xu, W. Yin, G.P. Hao, W.C. Li, Revealing an extended adsorption/insertion-filling sodium storage mechanism in petroleum coke-derived amorphous carbon, Adv. Sci. 11 (2024) 2407538.

[20] S. Dong, Y. Song, Y. Fang, G. Wang, Y. Gao, K. Zhu, D. Cao, Rapid carbonization of anthracite coal via flash joule heating for sodium ion storage, ACS Appl. Energy Mater. (2024) DOI: 10.1021/acsaem.1023c02975.

[21] X. Liu, H. Tao, C. Tang, X. Yang, Anthracite-derived carbon as superior anode for lithium/potassium-ion batteries, Chem. Eng. Sci. 248 (2022) 117200.

[22] Q. Meng, Y. Lu, F. Ding, Q. Zhang, L. Chen, Y.-S. Hu, Tuning the closed pore structure of hard carbons with the highest Na storage capacity, ACS Energy Lett. 4 (2019) 2608-2612.

[23] Z. Tang, R. Zhang, H. Wang, S. Zhou, Z. Pan, Y. Huang, D. Sun, Y. Tang, X. Ji, K. Amine, M. Shao, Revealing the closed pore formation of waste wood-derived hard carbon for advanced sodium-ion battery, Nat. Commun. 14 (2023) 6024.

[24] Y. Zhen, Y. Chen, F. Li, Z. Guo, Z. Hong, M.-M. Titirici, Ultrafast synthesis of hard carbon anodes for sodium-ion batteries, Proc. Natl. Acad. Sci. U.S.A. 118 (2021) e2111119118.

[25] C. Nita, B. Zhang, J. Dentzer, C. Matei Ghimbeu, Hard carbon derived from coconut shells, walnut shells, and corn silk biomass waste exhibiting high capacity for Na-ion batteries, J. Energy Chem. 58 (2021) 207-218.

[26] H. Fujimoto, K. Tokumitsu, A. Mabuchi, N. Chinnasamy, T. Kasuh, The anode performance of the hard carbon for the lithium ion battery derived from the oxygen-containing aromatic precursors, J. Power Sources 195 (2010) 7452-7456.

[27] M. Enterría, J.L. Figueiredo, Nanostructured mesoporous carbons: Tuning texture and surface chemistry, Carbon 108 (2016) 79-102.

[28] D. Cheng, X. Zhou, H. Hu, Z. Li, J. Chen, L. Miao, X. Ye, H. Zhang, Electrochemical storage mechanism of sodium in carbon materials: A study from soft carbon to hard carbon, Carbon 182 (2021) 758-769.

[29] H. He, J. He, H. Yu, L. Zeng, D. Luo, C. Zhang, Dual-interfering chemistry for soft-hard carbon translation toward fast and durable sodium storage, Adv. Energy Mater. 13 (2023) 2300357.

[30] Z. Jiang, Y. Zhao, W. Kang, B. Xing, H. Jiang, G. Huang, C. Zhang, Y. Cao, Anthracite-based reduced graphene oxide/antimony composites as anode materials for high performance sodium ion batteries, J. Alloys Compd. 925 (2022) 166631.

[31] M.K. Le, T.N. Tran, T.K.T. Huynh, V.H. Nguyen, D.T. Vo, V.M. Tran, M.L.P. Le, Development of vang danh anthracite as a cost-effective anode for sodium-ion batteries through a heat-treatment process, RSC Adv. 12 (2022) 29900-29907.

[32] B.-Y. Wang, J.-L. Xia, X.-L. Dong, X.-S. Wu, L.-J. Jin, W.-C. Li, Highly purified carbon derived from deashed anthracite for sodium-ion storage with enhanced capacity and rate performance, Energy Fuels 34 (2020) 16831-16837.

[33] H. Zeng, B. Xing, Y. Cao, B. Xu, L. Hou, H. Guo, S. Cheng, G. Huang, C. Zhang, Q. Sun, Insight into the microstructural evolution of anthracite during carbonization-graphitization process from the perspective of materialization, Int. J. Min. Sci. Technol. 32 (2022) 1397-1406.

[34] J. Wang, Y. Cui, Y. Gu, H. Xu, Y. Shi, Z. Ju, Q. Zhuang, Coal-based modified carbon for high performance sodium-ion battery, Solid State Ionics 368 (2021) 115701.

[35] Z. Zheng, S. Hu, W. Yin, J. Peng, R. Wang, J. Jin, B. He, Y. Gong, H. Wang, H.J. Fan, CO_2-etching creates abundant closed pores in hard carbon for high-plateau-capacity sodium storage, Adv. Energy Mater. 14 (2023) 2303064.

[36] J. Peng, H. Wang, X. Shi, H.J. Fan, Ultrahigh plateau-capacity sodium storage by plugging open pores, Adv. Mater. (2024) 2410326.

[37] K. Wang, F. Sun, H. Wang, D. Wu, Y. Chao, J. Gao, G. Zhao, Altering thermal transformation pathway to create closed pores in coal-derived hard carbon and boosting of Na^+ plateau storage for high-performance sodium-ion battery and sodium-ion capacitor, Adv. Funct. Mater. 32 (2022) 2203725.

[38] Z. Lu, J. Wang, W. Feng, X. Yin, X. Feng, S. Zhao, C. Li, R. Wang, Q.A. Huang, Y. Zhao, Zinc single-atom-regulated hard carbons for high-rate and low-temperature sodium-ion batteries, Adv. Mater. 35 (2023) 2211461.

[39] G. Zhao, T. Xu, Y. Zhao, Z. Yi, L. Xie, F. Su, Z. Yao, X. Zhao, J. Zhang, W. Xie, X. Li, L. Dong, C.-M.

Chen, Conversion of aliphatic structure-rich coal maceral into high-capacity hard carbons for sodium-ion batteries, Energy Storage Mater. 67 (2024) 103282.

[40] S. You, Q. Zhang, J. Liu, Q. Deng, Z. Sun, D. Cao, T. Liu, K. Amine, C. Yang, Hard carbon with opened pore structure for enhanced sodium storage performance, Energy Environ. Sci. 17 (2024) 8189-8197.

[41] J. Liu, Y. You, L. Huang, Q. Zheng, Z. Sun, K. Fang, L. Sha, M. Liu, X. Zhan, J. Zhao, Y.C. Han, Q. Zhang, Y. Chen, S. Wu, L. Zhang, Precisely tunable instantaneous carbon rearrangement enables low-working-potential hard carbon toward sodium-ion batteries with enhanced energy density, Adv. Mater. 36 (2024) 2407369.

[42] L. Quan, G. Yunzhi, W. Huiying, Investigation of pyrolysed anthracite as an anode material for sodium ion batteries, New J. Chem. 46 (2022) 13575-13581.

[43] R. Li, B. Yang, A. Hu, B. Zhou, M. Liu, L. Yang, Z. Yan, Y. Fan, Y. Pan, J. Chen, T. Li, K. Li, J. Liu, J. Long, Heteroatom screening and microcrystal regulation of coal-derived hard carbon promises high-performance sodium-ion batteries, Carbon 215 (2023) 118489.

[44] X. Chen, J. Tian, P. Li, Y. Fang, Y. Fang, X. Liang, J. Feng, J. Dong, X. Ai, H. Yang, Y. Cao, An overall understanding of sodium storage behaviors in hard carbons by an "adsorption-intercalation/filling" hybrid mechanism, Adv. Energy Mater. 12 (2022) 2200886.

[45] M. Liu, J. Zhang, Z. Sun, L. Huang, T. Xie, X. Wang, D. Wang, Y. Wu, Dual mechanism for sodium based energy storage, Small 19 (2023) 2206922.

[46] H. Deng, L. Wang, S. Li, M. Zhang, T. Wang, J. Zhou, M. Chen, S. Chen, J. Cao, Q. Zhang, J. Zhu, B. Lu, Radial pores in nitrogen/oxygen dual-doped carbon nanospheres anode boost high-power and ultrastable potassium-ion batteries, Adv. Funct. Mater. 31 (2021) 2107246.

[47] M. Liu, Y. Xing, J. Wang, D. Wang, L. Huang, X. Wu, Z. Liu, Y. Wu, Besides the capacitive and diffusion control: inner-surface controlled bismuth based electrode facilitating potassium-ion energy storage, Adv. Funct. Mater. 31 (2021) 2101868.

[48] M. Song, Z. Yi, R. Xu, J. Chen, J. Cheng, Z. Wang, Q. Liu, Q. Guo, L. Xie, C. Chen, Towards enhanced sodium storage of hard carbon anodes: regulating the oxygen content in precursor by low-temperature hydrogen reduction, Energy Storage Mater. 51 (2022) 620-629.

Declaration of competing interest

The authors declare that they have no known competing financial interests or personal relationships that could have appeared to influence the work reported in this paper.

Graphical abstract

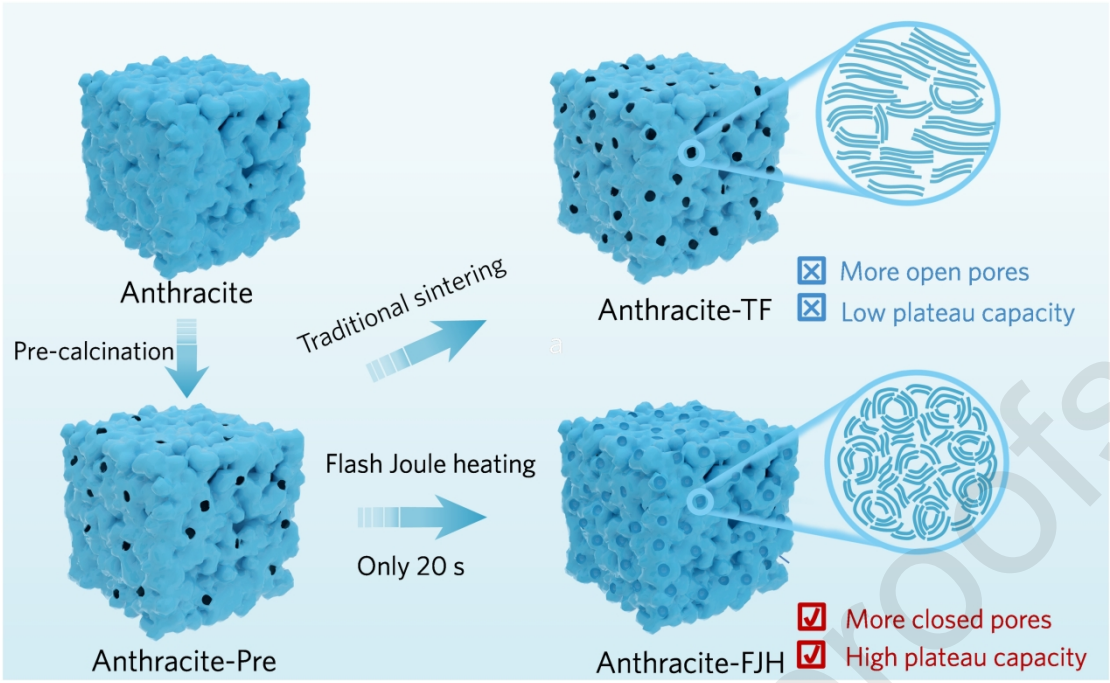

Anthracite-derived soft carbon rich in closed nanopores and significantly suppressed graphitization is synthesized through a kinetically controlled flash sintering strategy. This advancement has achieved a grealty extended low-voltage plateau for soft carbon, exhibiting a high Na^+-ion storage capacity of 309 mAh g^{-1} at 0.1 C. This work promotes the large-scale preparation and commercial application of low-cost soft carbon anodes for future sodium-ion batteries.

Highlights

1. Anthracite-derived soft carbon is synthesized through a flash sintering strategy.
2. Anthracite-derived soft carbon is rich in closed nanopores and reduced graphitization.
3. The soft carbon exhibits a significantly-extended low-voltage plateau below 0.1 V.
4. The soft carbon demonstrates a high Na^+-ion storage capacity of 309 mAh g^{-1} at 0.1 C.
5. Our work promotes the commercial application of high-capacity soft carbon anodes.